

Ground-Based Infrared Remote Sensing of Cloud Properties over the Antarctic Plateau. Part II: Cloud Optical Depths and Particle Sizes

ASHWIN MAHESH,* VON P. WALDEN,+ AND STEPHEN G. WARREN

Geophysics Program and Department of Atmospheric Sciences, University of Washington, Seattle, Seattle, Washington

(Manuscript received 26 August 1999, in final form 2 November 2000)

ABSTRACT

One full year of twice-daily longwave atmospheric emission spectra measured from the surface at 1-cm⁻¹ resolution are used to infer optical thicknesses and ice crystal sizes in tropospheric clouds over the Antarctic Plateau. The method makes use of the cloud's emissivity at 10- and 11- μm wavelength and the cloud's transmittance of stratospheric ozone emission in the 9.6- μm band. Knowledge of the cloud-base temperature and the vertical distributions of ozone and temperature is required; these are available at South Pole Station from radiosondes and ozonesondes. The difference in emissivity between 10 and 11 μm is sensitive to ice particle size because the absorption coefficient of ice varies greatly between these two wavelengths. The retrieval of optical depth (expressed as its value in the geometric-optics limit τ_g) is limited to $\tau_g < 5$, and the effective particle radii r_{eff} are distinguished only for $r_{\text{eff}} < 25 \mu\text{m}$, but 80% of the clouds observed have τ_g and r_{eff} in the retrievable range. These clouds over the Antarctic interior are found to be optically thin, usually with $\tau_g < 1$, in contrast to coastal clouds, which usually have $\tau_g > 20$. Most have r_{eff} in the range of 5–25 μm , with a mode at 15 μm . The retrieved r_{eff} is larger in summer than in winter, in agreement with in situ measurements. From November to April, r_{eff} was usually at least 10 μm , whereas, for a 3-month period in winter (July–September), no r_{eff} values greater than 25 μm were retrieved. The particle sizes retrieved from the infrared spectra are compared with dimensions of ice crystals falling to the surface and measured on photomicrographs. Effective spherical radii are computed from the photographs in three ways: equal area, equal volume, and equal volume-to-area ratio (V/A). Agreement with the r_{eff} derived from radiation measurements is best for equal-V/A spheres. The optical thicknesses and base heights inferred from the emission spectra agree qualitatively with the visual reports of the weather observers, in that the optically thicker clouds are usually reported as nimbostratus and clouds with the highest retrieved bases are reported as cirrus or cirrostratus. Stratus clouds tend to be reported as low; altostratus and altocumulus are intermediate in height.

1. Introduction

The climate of the Antarctic Plateau, like everywhere else on the earth, is strongly affected by clouds, and the clouds are, in turn, affected by other meteorological variables. The radiative effects of clouds are determined by the clouds' vertical location, optical thickness, and particle sizes. Radiation measurements correspondingly can be used to infer these properties.

We use longwave emission spectra measured at the surface (Walden et al. 1998) to infer cloud-base heights, optical thicknesses, and particle sizes. Measurements made twice daily through one full year are used to obtain

frequency distributions and seasonal cycles of these cloud properties. The measurements were made at only one location (South Pole Station), but because of the horizontal uniformity of the ice-sheet surface they are probably representative of a large area. We therefore offer them as an annual cycle of cloud properties for the East Antarctic Plateau, which should be useful for climate models of the Antarctic and surrounding regions (Simmonds 1990; Lubin et al. 1998). The determination of optical thicknesses and particle sizes is discussed in this paper (Part II); the method requires knowledge of the cloud-base height, obtained from Part I (Mahesh et al. 2001, this issue).

This study is related to others that develop remote sensing techniques using infrared spectral radiance measurements to determine cloud properties. A ground-based study of cirrus clouds was carried out in Wisconsin by Collard et al. (1995) during the First International Satellite Cloud Climatology Project Regional Experiment, Phase II. As in this study, the authors used window radiances together with model calculations to obtain cloud particle effective radii. These techniques

* Current affiliation: Goddard Earth Sciences and Technology Center, NASA Goddard Space Flight Center, Greenbelt, Maryland.

+ Current affiliation: Department of Geography, University of Idaho, Moscow, Idaho.

Corresponding author address: Stephen G. Warren, Dept. of Atmospheric Sciences, Box 351640, University of Washington, Seattle, WA 98195-1640.

E-mail: sgw@atmos.washington.edu

have also been applied to data from a coastal Antarctic station (Lubin 1994). A year-long dataset of cloud particle sizes and optical depths over the Antarctic Plateau has not previously been compiled, but short-duration studies have been conducted. Stone (1993) compared emissivities obtained from radiometersonde data with theoretically computed values for model clouds with various particle sizes and ice water contents (IWCs), but his study was based on only eight observations of winter clouds. His calculations were made with cloud particles represented as spheres with surface areas equal to those of the ice crystals, yielding radii of 4–16 μm and IWCs of 0.3–6 mg m^{-3} . Particle sizes have also been obtained previously from ice crystals collected over the plateau (Kikuchi and Hogan 1979), but these were limited to summer.

The determination of particle sizes and optical depths utilizes three pieces of spectral information: the transmittance of the cloud determined from spectral radiances in the 9.6- μm ozone band, and cloud emissivities obtained at two microwindows near 10 and 11 μm in the atmospheric window. The first two sections of this paper describe the procedures to determine these quantities. These are followed by the algorithm to determine particle sizes and optical depths using both the emissivities and transmittances. The annual cycle of these properties is then presented, followed by a discussion of the findings. The particle sizes obtained from the spectral measurements are compared with values obtained from near-simultaneous photographs of falling ice crystals.

2. Retrieval of ozone-band transmittance

a. Description of the retrieval technique

Ozone emission from above a cloud is often seen in our spectral measurements at the surface, because the cloud's optical thickness is usually not large enough to obscure this signal. Figure 1 shows a typical measurement sequence made under a cloud, in which emission from ozone above the cloud in the 9.6- μm band is detectable at the surface at all three viewing angles at which observations were made. However, at 75° the ozone signal is much less prominent than at 45°, because the path length through the cloud is much longer at 75°; the radiance itself is greater at the larger viewing angle because of cloud emission. Grund et al. (1990) showed that such incomplete attenuation of the ozone signal can be used to estimate cloud optical depths if the ozone signal is compared with the signal that would be recorded by the instrument in the absence of a cloud but under otherwise identical atmospheric conditions. This is accomplished by interpolating across the ozone band between frequencies that are dominated by emission from the cloud only. This background signal is subtracted from the observed spectrum within the ozone

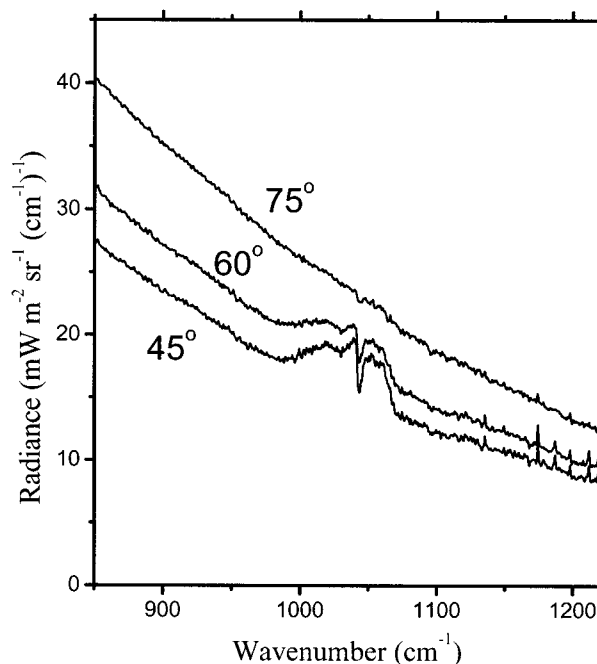


FIG. 1. Spectral radiance measurements in the 9.6- μm band of ozone made under a cloud on 22 Nov 1992 at three different viewing zenith angles. At larger viewing zenith angles, the radiance from the cloud is greater, but the signal of the overlying ozone emission is reduced by the increased path length through the cloud.

band. Then the resulting difference is used to determine the transmittance of the cloud.

The radiance I_{obs} received by the interferometer can be expressed as a sum of six terms. Four of these represent contributions to the measured radiance from ozone, and the other two are independent of the ozone profile. This can be written mathematically as

$$\begin{aligned}
 I_{\text{obs}} = & \int_{p_B}^{p_s} B[T(p)] \frac{d}{dp} t(p, p_s) dp \\
 & + r_c t(p_B, p_s) \int_{p_s}^{p_B} B[T(p)] \frac{d}{dp} t(p, p_B) dp \\
 & + t_c \int_0^{p_T} B[T(p)] \frac{d}{dp} t(p, p_s) dp \\
 & + \int_{p_T}^{p_B} t_o(p) B[T(p)] \frac{d}{dp} t(p, p_s) dp \\
 & + \epsilon_c B(T_B) t(p_B, p_s) + r_c t^2(p_B, p_s) \epsilon_s B(T_s), \quad (1)
 \end{aligned}$$

where $t(p_x, p_y)$ is the transmittance from pressure level x to pressure level y , p_B is the pressure at cloud base, p_T is the pressure at cloud top, p_s is the surface pressure, $B(T)$ is the Planck radiance at temperature T , ϵ_c is the cloud emissivity, r_c is the cloud base reflectance, t_c is the cloud transmittance, $t_o(p)$ is the cloud transmittance for downward emission by in-cloud ozone, and ϵ_s is the emissivity of snow. The infrared emissivity of snow is

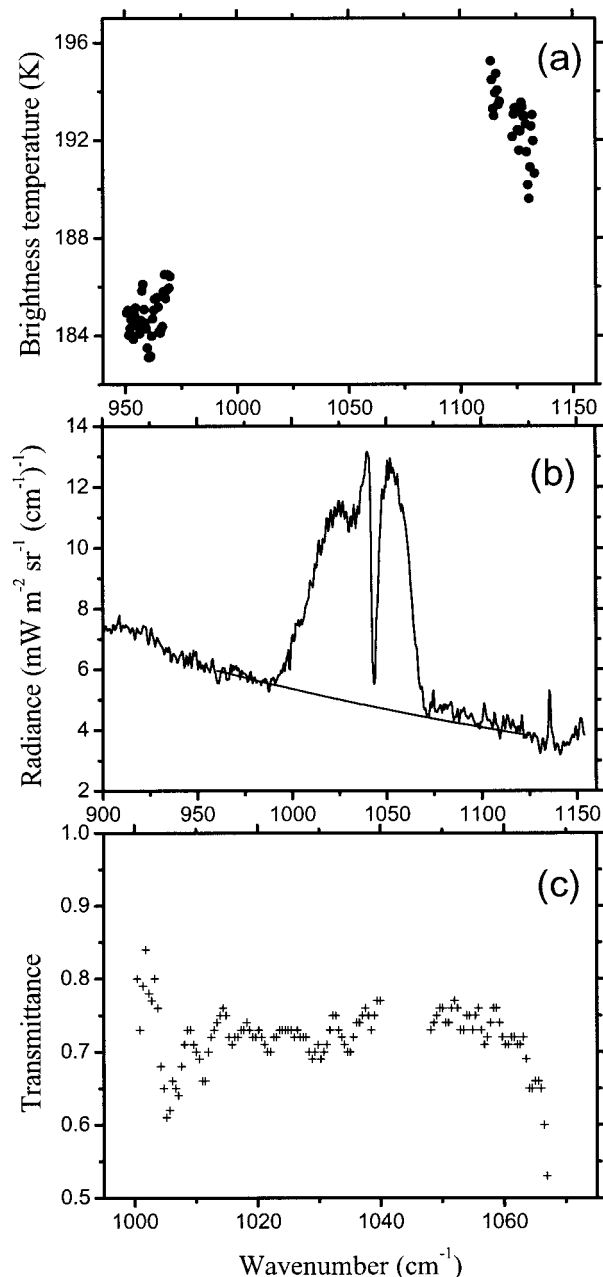


FIG. 2. The steps for determining transmittance from radiance measurements made on 14 Apr at 1200 UTC at a viewing angle of 45° . (a) Brightness temperatures are calculated in microwindows on either side of the ozone band. (b) The background radiance from nonozone sources is estimated by interpolating across the band using the brightness temperatures. (c) After subtracting out the contributions of ozone above and below the cloud, the transmittance of the cloud is estimated at numerous wavenumbers within the band.

greater than 0.98 in the $11\text{-}\mu\text{m}$ window (Dozier and Warren 1982; Grenfell 1998). As a result, very little cloud radiance is reflected between the surface and cloud base, and the contribution of multiple reflections to the observed downward radiance can be ignored.

The first term on the right side of Eq. (1) is the down-

ward emission by ozone in the atmosphere below the cloud. Part of the upward emission from this ozone is reflected downward by the cloud; this radiance is term 2. The third term is the fraction of the emission from ozone above the cloud that is transmitted through the cloud to the surface. The fourth term is the downward emission from ozone within the cloud itself, the fifth term is the nonozone contribution to radiance from the cloud (i.e., emission by ice crystals), and the sixth term is the portion of the upward radiance from the ground that is reflected back to the instrument by the cloud.

Term 1 can be calculated using a radiative transfer model if the cloud-base height (from Part I) and the ozone concentration as a function of altitude are known. (The vertical profile of ozone over the South Pole is measured at least once per week by ozonesondes throughout the year. During the spring when the ozone concentration changes more rapidly, ozonesondes are launched every three days.) Term 2 is usually much smaller than term 1, because the reflectance of the cloud at $9.6\text{ }\mu\text{m}$ is at most 2%–3%. Ozone in the lower troposphere is less than 10% of the total column ozone and is usually much less because the clouds are low. So term 1 is small, and term 2 is only about 2% of term 1; therefore term 2 is ignored.

b. Determination of the background signal

To obtain the cloud transmittance, the background radiance is subtracted from the measured radiance. The combination of terms 1, 5, and 6 is the background radiance, which would be observed even if the atmosphere above the cloud base contained no ozone. The background is estimated by interpolating across the ozone band, between frequencies at which the signal is dominated by emission from the cloud. The measured radiances are first converted to brightness temperatures in two narrow microwindows on either side of the ozone band, one at $950\text{--}970\text{ cm}^{-1}$ and the other at $1118\text{--}1135\text{ cm}^{-1}$ (Fig. 2a). (Microwindows are small spectral intervals over which there is negligible emission from atmospheric gases.) This allows one to obtain the spectral signature of the cloud only. The microwindows are chosen to be near the ozone band, so that cloud emissivity at these wavenumbers is nearly the same as the cloud emissivity within the ozone band. Averaging over many wavenumbers in the microwindows reduces the uncertainties in the brightness temperature resulting from noise in the interferometric measurements.

The background radiances at wavenumbers within the ozone band are obtained by interpolating between the mean brightness temperatures in the microwindows (Fig. 2b). The mean value is used, rather than the minimum value, because the minimum is biased toward low values because of instrumental noise. The interpolation is performed over brightness temperature rather than radiance so that any variation in emissivity from one

side of the ozone band to the other is included in the calculation of the background.

c. Adjustment of the background radiance

If the atmosphere below the cloud base were isothermal and at the same temperature as the cloud base, then the absorption of cloud radiance by ozone below the cloud (which determines t in term 5) would be exactly balanced by emission from this same ozone, and the interpolated background radiance would correctly account for emission from ozone below the cloud: term 1 in Eq. (1). In actuality, the ozone below the cloud is distributed over a range of atmospheric temperatures, usually different from the cloud-base temperature. The background radiance obtained by interpolation therefore does not accurately remove the contribution of terms 1, 5, and 6 and requires adjustment. To estimate this adjustment to the background, we calculate the emission from ozone below the cloud by a radiative transfer model in two ways, one using the actual vertical profile of temperature and another using an isothermal temperature profile with all temperatures set to equal the cloud-base temperature. From the interpolated background radiance, the latter is subtracted, then the former is added to yield the true background.

d. Accounting for ozone emission within the cloud

Although the cloud-base heights are known from the radiance-ratioing method (described in Part I), the cloud-top heights are unknown. However, this limitation is not serious, because the tropospheric ozone is usually less than 10% of the total ozone. If all the ozone within the cloud were at the cloud base, then its emission would not be attenuated by the cloud. On the other hand, if all the ozone within the cloud were at the top of the cloud, then the attenuation of its emission would be similar to the cloud's attenuation of emission from gases above the cloud. We therefore assume that the transmittance of the cloud to ozone emission within the cloud lies halfway between these extremes; we set $t_o(p) \approx (1 + t_c)/2$ in term 4 and take it outside the integral. Because only a small portion of the total ozone signal is derived from the troposphere and the cloud thickness is only a fraction of the tropospheric thickness, emission from the ozone within the cloud is small, and the portion transmitted by the cloud can be adequately estimated using this assumption and any reasonable estimate of the cloud-top height. Radiosonde data suggest that the cloud thicknesses are a few hundred to a few thousand meters, so for evaluation of terms 3 and 4 a cloud thickness of 1 km is assumed.

e. Calculation of the cloud transmittance

The integrals in terms 3 and 4 are computed using a radiative transfer model. Using the assumed value for

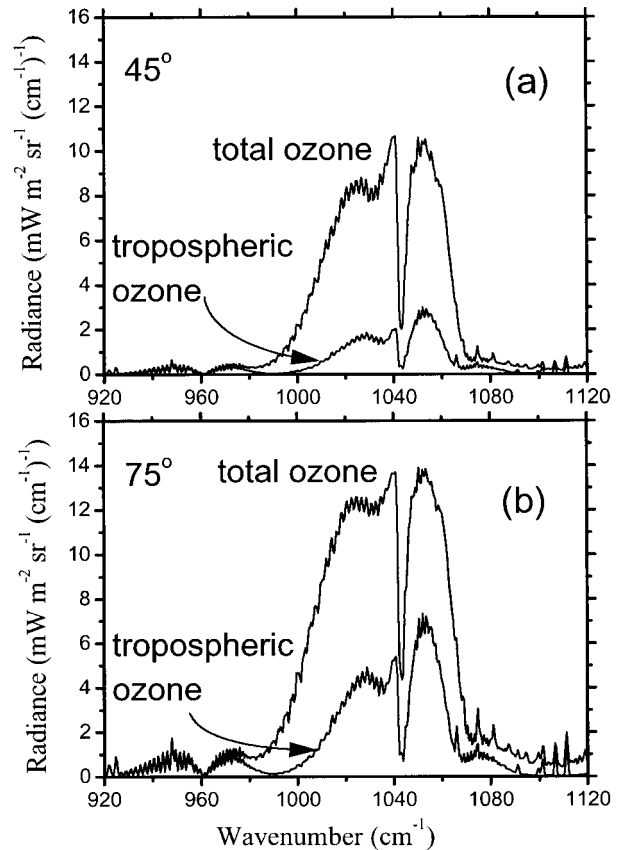


FIG. 3. Contribution of tropospheric ozone to downward radiance at the surface, computed by LBLRTM. Tropospheric ozone is usually less than 10% of the total ozone in the atmosphere. (a) At small viewing zenith angles the tropospheric contribution to the total radiance at all wavenumbers in the 9.6- μm band remains small. (b) At larger viewing angles, the differences in atmospheric transmission between wavenumbers in the band become more important. At wavenumbers near the center of the band, where atmospheric opacity is greater, more than one-third of the ozone signal is from the troposphere. Near the edges of the band, at the more far-sighted wavenumbers, tropospheric contributions are small.

t_o , the remaining unknown in Eq. (1) is the transmittance t_c of the cloud. After combination of the background terms, Eq. (1) can be written as

$$I_{\text{obs}} - I_{\text{bkg}} = t_c \Sigma_3 + \left(\frac{1 + t_c}{2} \right) \Sigma_4, \quad (2)$$

where Σ_3 and Σ_4 are the integrals in terms 3 and 4 [after removing $t_o(p)$ from the integrand of term 4]. Equation (2) is then solved for t_c at each wavenumber (Fig. 2c).

f. Uncertainty in the cloud transmittance

The transmission values in Fig. 2c show some variability over the range of wavenumbers at which they are calculated. This variability is partly due to the variation in e -folding distance of transmission into the atmosphere at different wavenumbers within the band.

Figure 3 shows the contribution of tropospheric ozone to the total clear-sky emission, calculated using the Line-By-Line Radiative Transfer Model (LBLRTM; Clough et al. 1992) at viewing zenith angles of 45° and 75° . Between 1025 and 1050 cm^{-1} , the e -folding distance is ~ 140 Dobson Units (DU); for 1000 – 1025 cm^{-1} , it is about 70 DU; and for 975 – 1000 cm^{-1} , it is about 3 DU (Houghton 1991). At 45° , tropospheric ozone contributes at most 10% of the radiance at all wavenumbers within the band, whereas at 75° , only the wavenumbers in the far wings of the band meet this criterion. To minimize the uncertainty from lack of knowledge of the cloud-top height, we estimate the transmittance of the cloud as the average value obtained at all wavenumbers at which tropospheric ozone contributes no more than 10% to the total ozone signal. At 45° , we use transmittance values near the center of the band (~ 1018 – 1040 cm^{-1}), but at 75° we use the longwave wing (1008 – 1020 cm^{-1}), and at 60° we use an intermediate set.

3. Window emissivities

Figure 4 shows absorption, scattering, and extinction efficiencies (Q_{abs} , Q_{scat} , and Q_{ext}) at six different microwindows in the $11\text{-}\mu\text{m}$ window region, over a range of particle sizes, computed using Mie theory (Wiscombe 1979, 1980) for ice spheres. The complex refractive index of ice was taken from Warren (1984). The microwindows were chosen at locations where absorption by atmospheric gases is negligible. The absorption efficiency varies with cloud particle size at all wavenumbers, but is more sensitive at some wavenumbers than at others. Variation in Q_{abs} with particle size is necessary to determine the cloud particle effective radius. Although there is sufficient variation at all wavenumbers to distinguish particle radii less than $10\text{ }\mu\text{m}$, it is only at 988 cm^{-1} that variation in Q_{abs} continues monotonically to radii of 20 – $30\text{ }\mu\text{m}$. The ability to obtain unique solutions, as well as the two extremes of sensitivity to a broad range of particles (1 – $25\text{ }\mu\text{m}$) can be achieved by using just the two microwindows at 903 and 988 cm^{-1} . Further, most of the variation in emissivity between 810 and 1000 cm^{-1} occurs between 903 and 988 cm^{-1} (Fig. 5), making these wavenumbers adequately representative of the variation in absorption by ice across the window.

Figures 6a,b show calculations of cloud emissivity at $\nu = 903$ and 988 cm^{-1} . Extinction efficiencies, single-scattering albedos, and phase-function moments were calculated for ice spheres using Mie theory. Morley et al. (1989) had previously reported that clouds over the Antarctic Plateau were mostly made of ice particles. For this work, the spectra were all analyzed as if the clouds consisted of ice crystals, although some of the summer clouds probably contained supercooled liquid water droplets. Cloud emissivities were computed using the Discrete Ordinates Radiative Transfer code (DISORT;

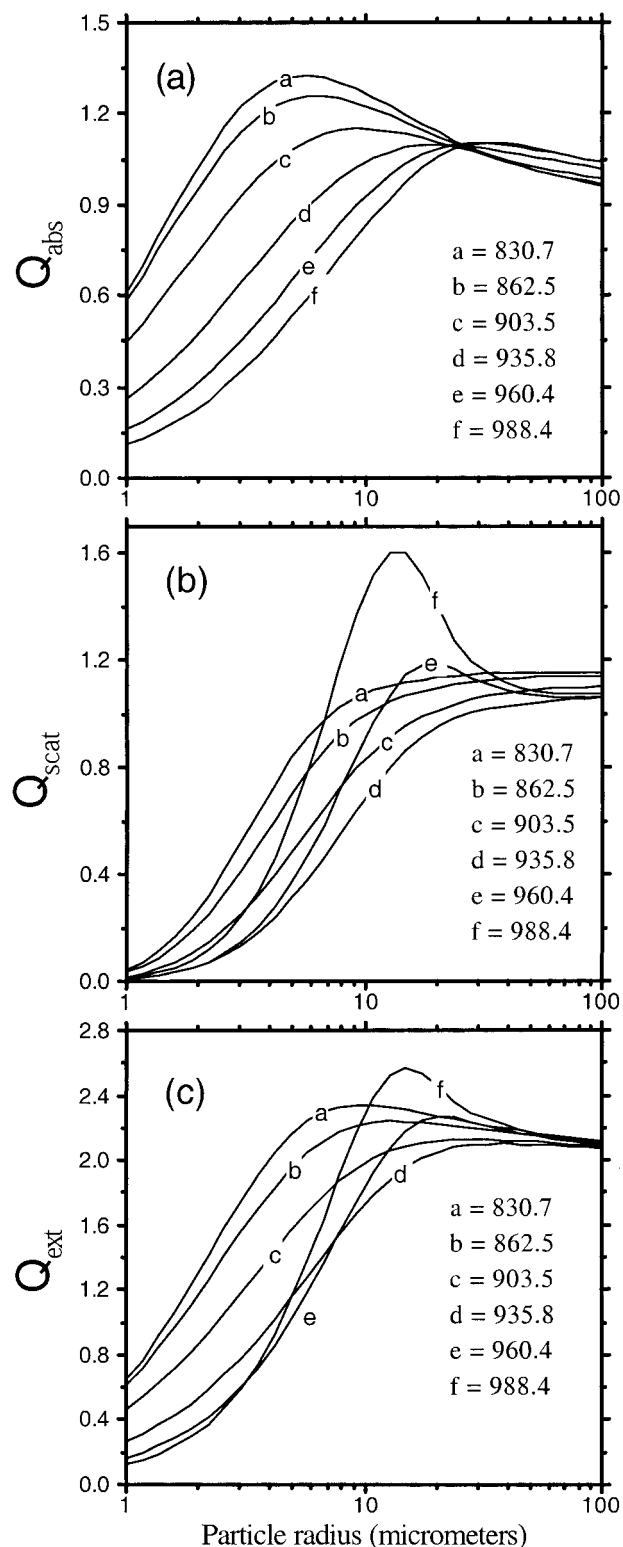


FIG. 4. (a) Absorption efficiency Q_{abs} , (b) scattering efficiency Q_{scat} , and (c) extinction efficiency Q_{ext} as functions of cloud particle size at six different microwindows (labeled a–f, cm^{-1}) in the $11\text{-}\mu\text{m}$ window region.

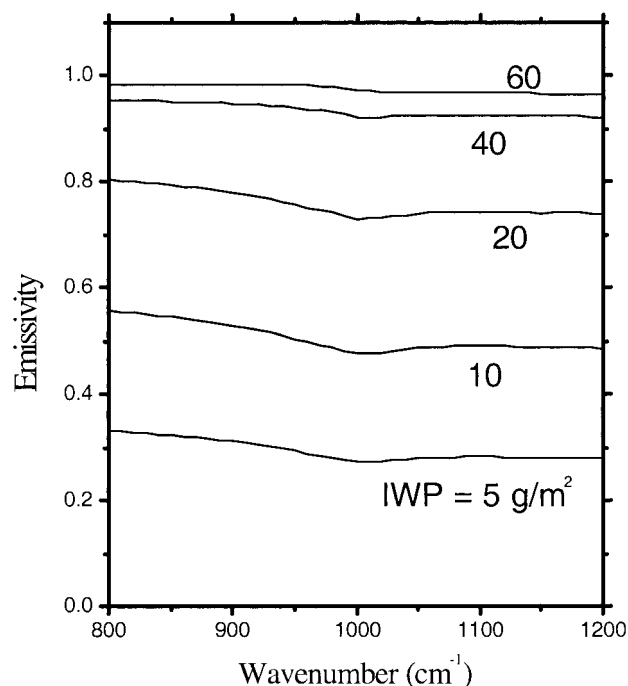


FIG. 5. Spectral emissivity for ice clouds between 800 and 1200 cm^{-1} , computed for several values of cloud ice water path and $r_{\text{eff}} = 15 \mu\text{m}$.

Stamnes et al. 1988). Thermal emission radiances I_{calc} from clouds were computed using 40 streams in DISORT; the cloud emissivities were then computed using cloud base temperatures T_c obtained with information from Part I as

$$\varepsilon = \frac{I_{\text{calc}}}{B(T_c)}. \quad (3)$$

However, I_{calc} includes not only emission from the cloud but also emission from the surface, which is reflected back to the instrument by the cloud. Therefore, the emissivity obtained from Eq. (3) is an “effective” emissivity, which includes reflection, which in the infrared is typically about 2%. Obtaining the effective emissivity using Eq. (3) and implicitly including this additional radiance makes the calculations comparable to our measurements of downward radiance, which also include reflection. For the DISORT computation, the snow surface temperature was set equal to the cloud-base temperature, but because of the small reflectance of the cloud this assumption does not significantly alter the results.

Mie and DISORT calculations were made for clouds with several different particle radii (r_{eff} between 0.5 and 100 μm) and many values of optical depth in the geometric-optics limit (τ_g between 0.01 and 100). The “effective radius” r_{eff} is the area-weighted mean radius, introduced by Hansen and Travis (1974). The optical depth in the geometric-optics limit is used to describe the clouds because it is a quantity that is independent

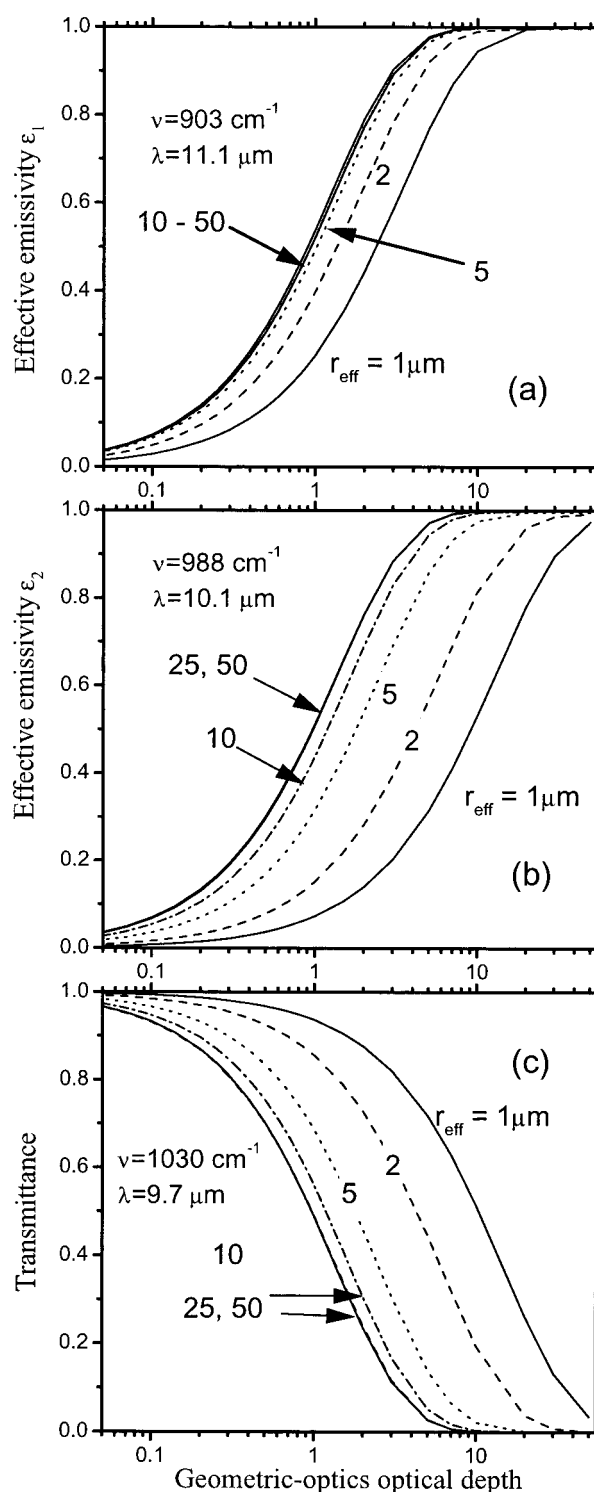


FIG. 6. Contours of (a) cloud effective emissivity at 903 cm^{-1} , (b) cloud effective emissivity at 988 cm^{-1} , and (c) cloud transmittance in the 9.6- μm ozone band for different particle sizes, computed using Mie theory and DISORT. In each case, six different curves are shown for particle radii of 1–50 μm .

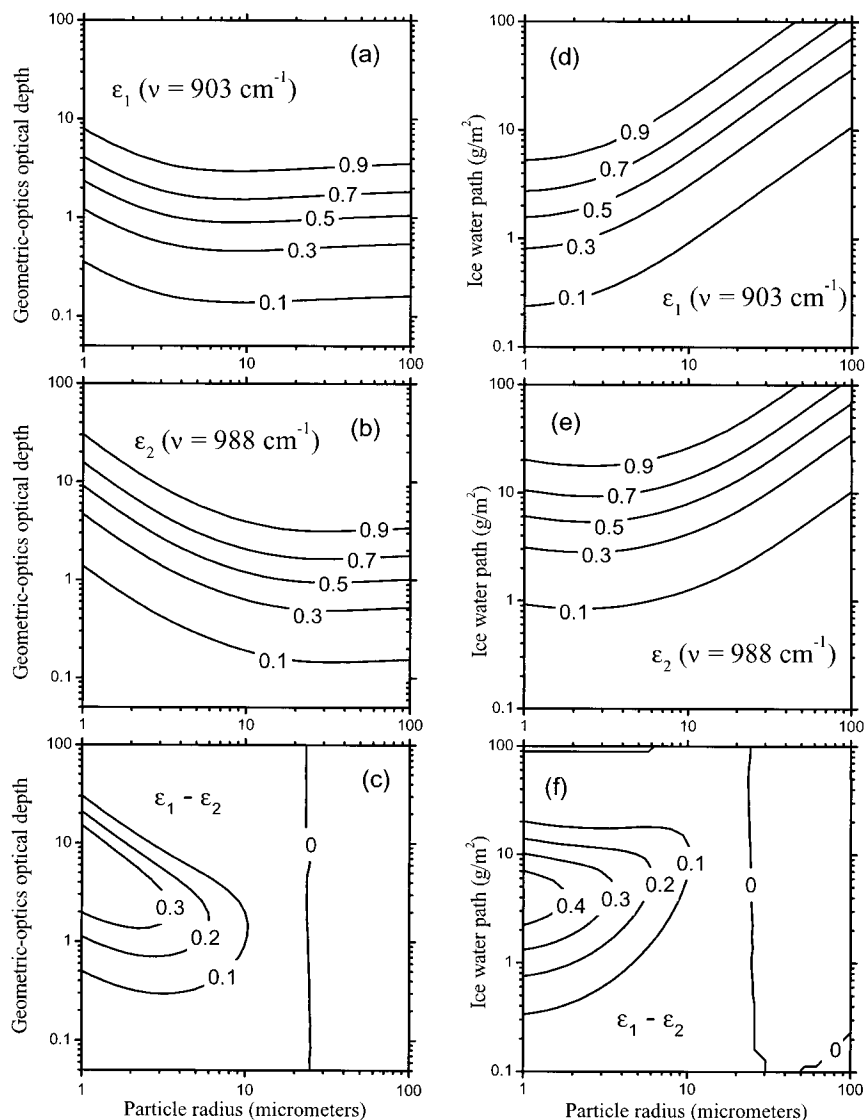


FIG. 7. (a), (b), (d), (e) Emissivities at 903 and 988 cm^{-1} , plotted as functions of particle radius and either (left) cloud optical depth or (right) ice water path. (c), (f) Difference in emissivities at these two microwindows. A negative or zero emissivity difference implies particle radius greater than 25 μm , whereas a positive difference implies smaller particles.

of wavenumber. For particle sizes greater than 5 μm , the emissivity at 903 cm^{-1} (ϵ_1) is insensitive to particle size, whereas at 988 cm^{-1} the sensitivity to particle size extends up to particles of $r_{\text{eff}} = 25 \mu\text{m}$. Figure 6c shows that transmittance in the ozone band (t_c) is as sensitive to particle size as the emissivity at 988 cm^{-1} (ϵ_2). This variation in sensitivity with wavenumber means that the two desired quantities (r_{eff} and τ_g) can be inferred from the three measured quantities (ϵ_1 , ϵ_2 , and t_c).

The computed emissivities and their difference ($\epsilon_1 - \epsilon_2$) are shown as contour plots in Fig. 7 over a range of cloud thicknesses (expressed both as optical depths and as ice water paths). For r_{eff} greater than 25 μm , $\epsilon_1 - \epsilon_2$ is negative; for r_{eff} less than 25 μm it is positive.

Over a range of particle sizes and geometric optical depths, the two emissivities together indicate specific particle radii and optical depths. Model computations of those quantities can then be compared with observations made under the cloud to obtain r_{eff} and τ_g .

The effective emissivities are determined from the spectral radiance measurements and the cloud-base temperature. To reduce the effect of random measurement errors, the emissivities ϵ_1 and ϵ_2 for each observation are obtained as averages over 3- cm^{-1} intervals centered at 903 and 988 cm^{-1} , respectively, rather than at single wavenumbers. The temperature at cloud base is obtained from radiosonde data together with the cloud-base height determined in Part I.

4. Minimization routine

From each measured radiance spectrum, we obtain three different quantities, the two effective emissivities and the transmittance in the ozone band. These quantities can now be compared with corresponding values computed over a wide range of particle sizes and optical depths. This approach—comparing observed emissivities and transmittances to model calculations—is similar to that used by others (Smith et al. 1993; DeSlover et al. 1999), but it uses fewer microwindows in the atmospheric windows than they did.

In the minimization algorithm, the emissivities and transmittance are weighted according to the reciprocal of the relative magnitude of their uncertainties. Uncertainty in cloud-base height determined by radiance ratioing propagates to uncertainty in cloud-base temperature and thereby to uncertainty in emissivities determined at the two wavenumbers. Uncertainties in ozone-band transmittance also result from errors in spectral radiance measurements within the band, and from uncertainties in determining the emission from stratospheric ozone. Day-to-day variability in stratospheric ozone emission is nearly constant at about $1 \text{ mW m}^{-2} \text{ sr}^{-1} (\text{cm}^{-1})^{-1}$ (1 radiance unit; RU) throughout the year (Fig. 8). However, the monthly average emission undergoes a large seasonal cycle, ranging from 16–18 RU in summer to 5 RU in winter and spring. As a result, the uncertainties in ozone transmittance values due to uncertainty in the ozone profile are larger in winter and spring ($\sim 20\%$) than in summer and autumn ($< 10\%$).

Uncertainties in the emissivities were estimated to be typically 5%–8% of the emissivity values themselves; these result mostly from uncertainties in cloud-base temperature and uncertainties due to measurement error. Uncertainties in the measured radiances were determined by Walden (1995). Errors in cloud-base temperature correspond primarily to errors in cloud-base heights, which are estimated in Table 1 of Part I. Both sources of uncertainty are, however, correlated across the window region; that is, errors in ε_1 are correlated with errors in ε_2 . As a result, the difference $\Delta\varepsilon \equiv (\varepsilon_1 - \varepsilon_2)$ can be estimated more accurately than either ε_1 or ε_2 . The algorithm to minimize the differences between observations and calculations takes advantage of this.

The quantities ε_1 , $\Delta\varepsilon$, and t_c from the observations form a 3-element vector, indicated by $[\]$, that is compared with corresponding vectors calculated for all possible combinations of r_{eff} and τ_g . The minimization algorithm computes the rms error:

$$[\varepsilon_1, \Delta\varepsilon, t_c]_{\text{observations}} - [\varepsilon_1, \Delta\varepsilon, t_c]_{\text{calculations}}.$$

In the minimization process, the individual quantities in the vectors are then weighted according to their relative accuracies; $\Delta\varepsilon$ is weighted 5 times as much as ε_1 . The relative accuracy of ε_1 and t_c is determined as follows. The emissivity at 903 cm^{-1} depends on the as-

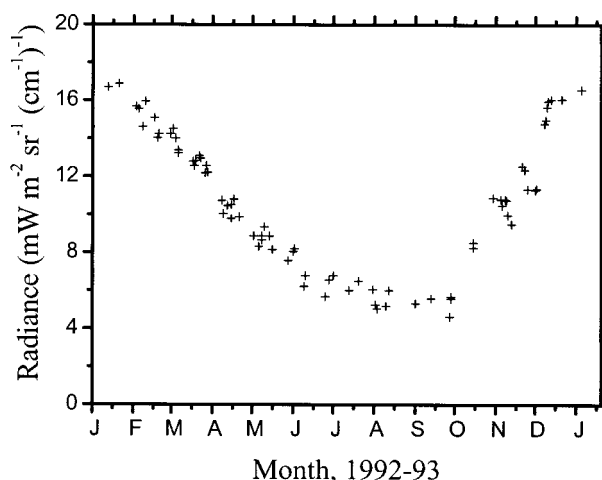


FIG. 8. Clear-sky radiances in the $9.6\text{-}\mu\text{m}$ ozone band are shown for $\nu = 1035 \text{ cm}^{-1}$. The values range from summertime highs of about 17 RU to springtime lows of 4–6 RU. Day-to-day variability in the ozone emission is about 1 RU throughout the year, leading to greater uncertainties in ozone transmittance in winter and spring.

sumed cloud-base temperature; uncertainties in this quantity result from uncertainties in the temperature. The cloud-base temperature is perturbed by its estimated uncertainty of 3 K, and the corresponding change in ε_1 is determined. The transmittance in the ozone band is most sensitive to day-to-day variation in stratospheric ozone emission. For each observation made under cloudy skies, the uncertainty in transmittance due to the variability in stratospheric ozone emission is determined. Uncertainties in ε_1 and t_c are then compared and assigned relative weights. The combination of particle radius and geometric optical depth is chosen such that the weighted combined difference in the measured and calculated values of ε_1 , $\Delta\varepsilon$, and t_c is minimized. The values of particle radius and geometric optical depth are determined at all viewing angles. When the same cloud is seen at more than one viewing angle, the angle at which the transmittance is closest to 0.5 is used. This is because τ is most accurately determined where the derivative $d[\log(\tau \sec\theta)]/dt$ is least, which occurs at $t = 0.5$.

5. Results

Figure 9 shows the optical depths and ice water paths (IWP) obtained for each cloud during the year; Fig. 10 shows histograms of the same quantities. These are related by

$$\tau_g = \frac{3}{2} \frac{\text{IWP}}{r_{\text{eff}} \rho_{\text{ice}}}, \quad (4)$$

where ρ_{ice} is the density of pure ice, 917 kg m^{-3} . Optical depths are shown for all observations in which clouds were detected, but IWP are shown only for those ob-

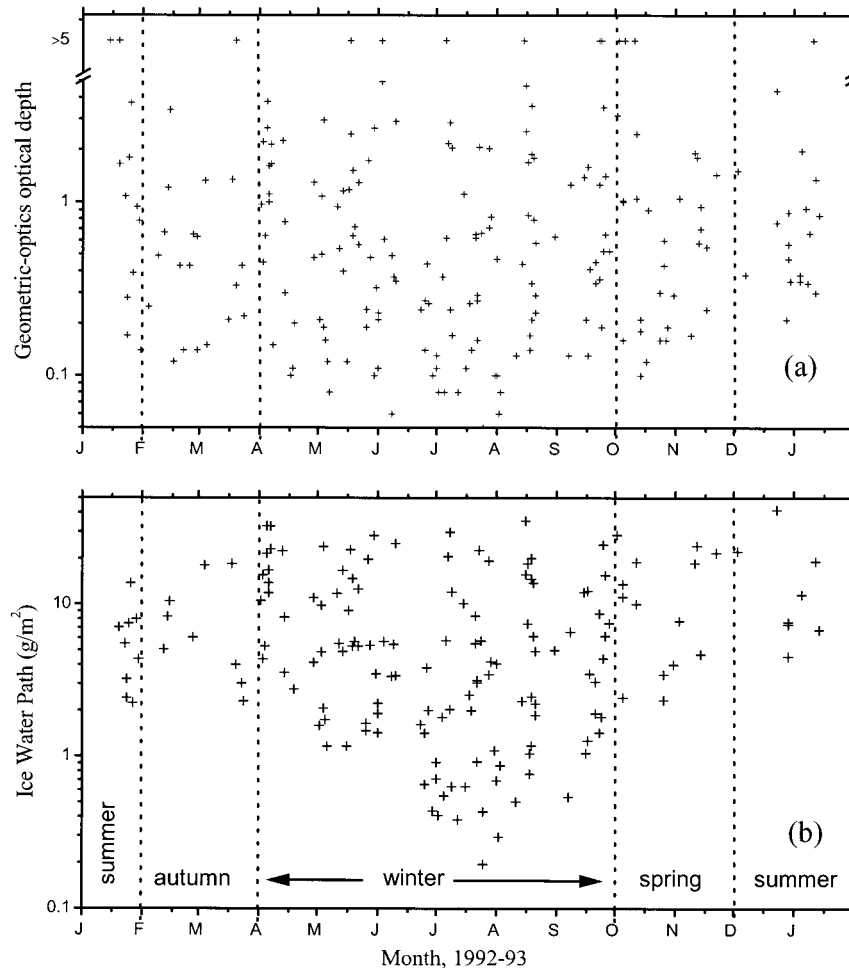


FIG. 9. (a) Cloud optical depths in the geometric-optics limit and (b) ice water paths at the South Pole during 1992–93. Tick marks indicate the beginning of each month. Both thick and thin clouds are observed during all seasons. Optical depths are not uniquely determined for extremely thick clouds ($\tau_g > 5$); for these cases, only a lower limit is indicated. Ice water paths are shown only for cases in which both the optical depth and the particle radii were uniquely determined; about 75% of the observations met this criterion.

servations in which both particle size and optical depth could be determined. This was possible in three-fourths of the observations; in other cases, only a lower limit to either the optical depth or particle size could be obtained. Fewer than 10% of the clouds have $\tau_g > 5$, and about two-thirds have $\tau_g < 1$. The histograms show frequencies of observations separately for the winter and nonwinter months. Optical depths greater than 5 are twice as common in nonwinter months as in winter months.

Stone (1993) obtained similar values from radiometer-sonde measurements of upward and downward fluxes at the South Pole. He determined cloud-top and -base heights of eight wintertime clouds from vertical profiles of flux and temperature. He then estimated the emissivity and optical depths of the clouds by comparing the observations to model comparisons made at $10.8\text{-}\mu\text{m}$ wavelength; he found the average emissivity to be 0.6

and the average optical depth to be 1.0. These values are consistent with our results. Stone's model calculations, which used ice spheres, implied particle radii from 4 to $16\text{ }\mu\text{m}$ (also consistent with our results shown below), and IWCs of 0.3 to 6 mg m^{-3} .

We considered the possibility that the smallest optical depths we obtain may in fact be of Pinatubo aerosol rather than clouds, but rejected it. The infrared optical depths of stratospheric aerosol are between one-quarter and one-half of the visible optical depths (Lacis et al. 1992), which through most of 1992 were about 0.1 or less (E. Dutton 1994, personal communication); measurements of aerosol under cloud-free conditions lie within our threshold for cloud detection (optical depth of 0.06 or less; see Part I).

Figure 10 shows a predominance of thin clouds ($\tau_g < 2$). This finding contrasts with results from the coast of Antarctica, where Ricchiazzi et al. (1995), using solar

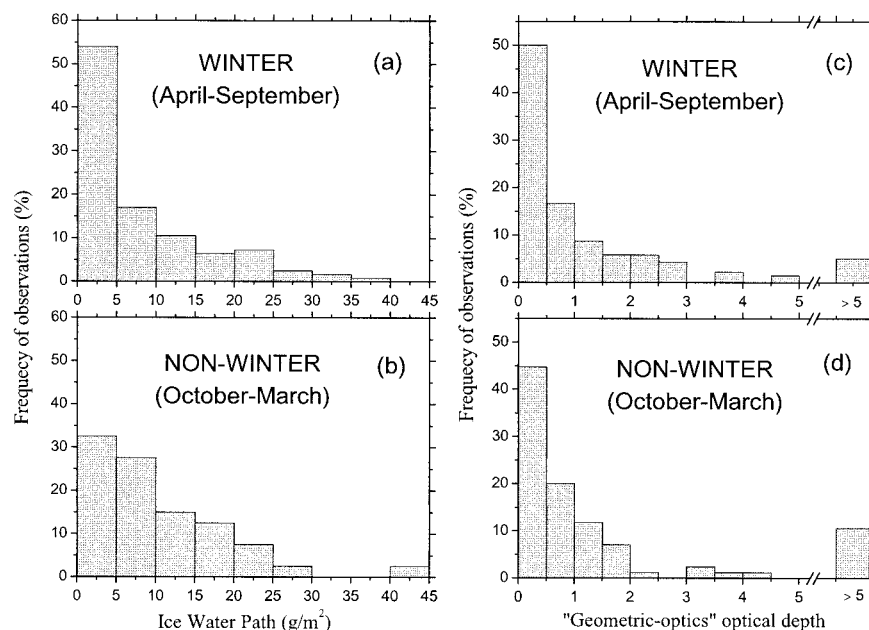


FIG. 10. Histograms of (a), (b) ice water path and (c), (d) optical depth at the South Pole during 1992, shown for the winter and nonwinter months separately. About 5% of the clouds had optical depths too large to be uniquely determined ($\tau_s > 5$). Approximately 65% of the clouds have $\tau_s < 1$. Ice water paths are shown only for those cases in which both particle size and optical depth could be uniquely determined; about 75% of the observations met this criterion.

irradiance data from a ground-based multichannel radiometer, found $\tau_s \sim 20$ for clouds at Palmer Station (65°S, 64°W). Such clouds are effectively semi-infinite in the infrared; our methods would therefore not be appropriate for determining their optical thicknesses.

The effective particle radii r_{eff} obtained from the spectral measurements are shown in Fig. 11; histograms of these values are shown, for winter and nonwinter

months separately, in Fig. 12. The median value of r_{eff} , computed including particles larger than 25 μm , is 15.2 μm . As suggested by Fig. 7, when r_{eff} is greater than 25 μm an accurate determination of r_{eff} is not possible, so only a lower limit is indicated in these cases. Approximately 20% of the clouds have retrieved $r_{\text{eff}} > 25 \mu\text{m}$. Clouds with $r_{\text{eff}} > 25 \mu\text{m}$ are rarely seen in winter, and clouds with $r_{\text{eff}} < 10 \mu\text{m}$ are rarely seen during the

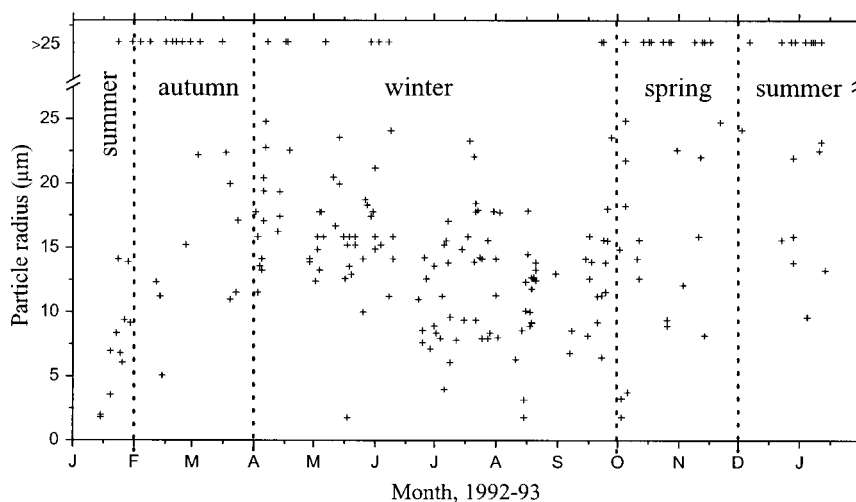


FIG. 11. Effective particle radii r_{eff} for clouds over the South Pole during 1992-93. Large particle radii are observed mostly in the summer; for four winter months, Jun-Sep, all clouds had $r_{\text{eff}} < 25 \mu\text{m}$. Particle sizes greater than 25 μm are not accurately determined; for these clouds, only a lower limit to r_{eff} is indicated.

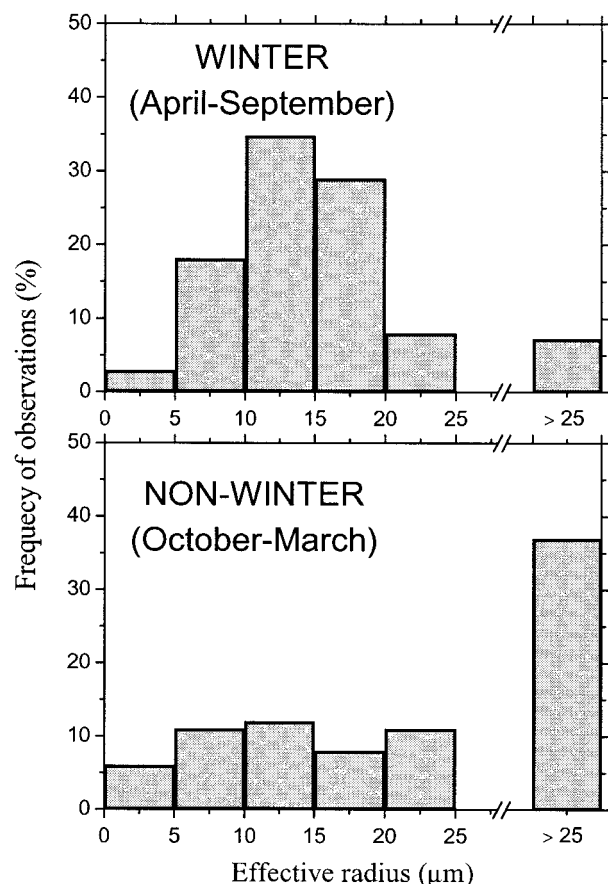


FIG. 12. Histograms of effective radii obtained at the South Pole during 1992, shown for the winter and nonwinter months separately. The median particle size for the entire year is $15.2 \mu\text{m}$. For $r_{\text{eff}} > 25 \mu\text{m}$, only a lower limit to r_{eff} is determined.

rest of the year. Lubin and Harper (1996) estimated effective radii using the Advanced Very High Resolution Radiometer channels at 11 and $12 \mu\text{m}$ and also found summer crystals to be larger than those in the winter. However, the values they obtained (mean r_{eff} of $12.3 \mu\text{m}$ in summer and $5.6 \mu\text{m}$ in winter) are smaller than the values of r_{eff} we obtain. This may be because crystals at cloud top are smaller than at cloud bottom. Precipitating ice crystals in summer were measured at South Pole Station by Kikuchi and Hogan (1979). For the 1200 crystals they sampled, the average c -axis length was $90 \mu\text{m}$, and the ratio c/a typically varied between 2.5 and 5.5; we relate these dimensions to an effective radius in section 6a.

Uncertainties in the emissivities at 903 and 988 cm^{-1} and transmittance in the ozone band produce uncertainties in the derived particle radius and optical depth. The uncertainties in the emissivities and transmittance were estimated, and the particle radius r'_{eff} and optical depth τ'_g were computed after the values of ε_1 , ε_2 , and t_c were perturbed by these uncertainties and were compared with r_{eff} and τ_g , respectively. The “resolution” of r_{eff} and τ_g was then determined as $|\ln(r_{\text{eff}}/r'_{\text{eff}})|$ and $|\ln(\tau_g/\tau'_g)|$, respectively, and are shown in Fig. 13. For small values of resolution, the resolution is the same as the fractional uncertainty; for example, the 0.2 contour means 22% uncertainty, and the 0.5 contour means 65%

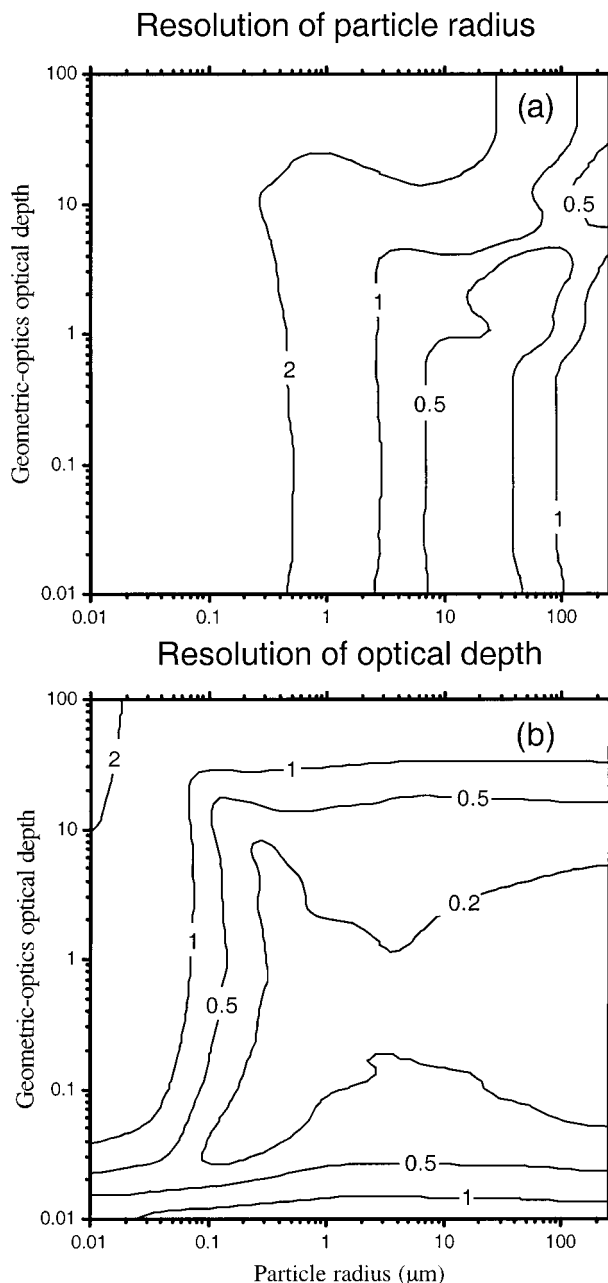


FIG. 13. Relative uncertainty in determination of (a) particle radius and (b) optical depth due to uncertainty in estimation of window emissivities and ozone-band transmittance. For a specified τ_g , r_{eff} combination, emissivities ε_i and transmittance t were calculated; they were perturbed to ε'_i and t' using estimated uncertainties in measured radiance and temperature. These perturbed values ε'_i and t' were used to infer cloud properties (τ'_g , r'_{eff}). The contours plotted are of $|\ln(r_{\text{eff}}/r'_{\text{eff}})|$ and $|\ln(\tau_g/\tau'_g)|$; for small $\Delta\tau_g$ and Δr_{eff} they are equivalent to $\Delta\tau_g/\tau_g$ and $\Delta r_{\text{eff}}/r_{\text{eff}}$, where $\Delta\tau_g \equiv |\tau_g - \tau'_g|$ and $\Delta r_{\text{eff}} \equiv |r_{\text{eff}} - r'_{\text{eff}}|$.

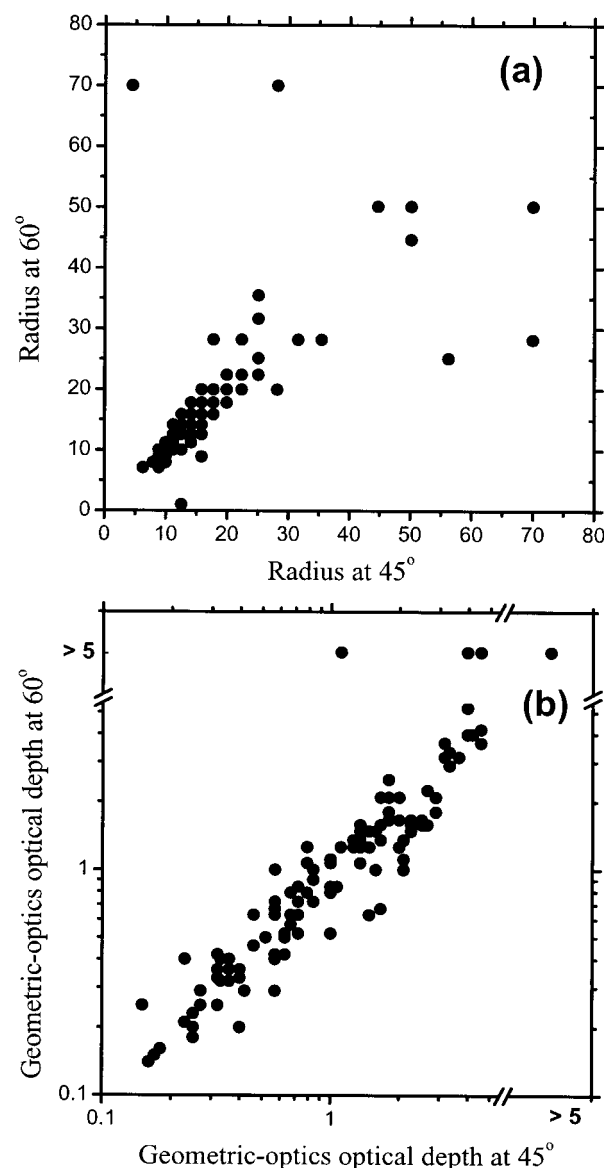


FIG. 14. Comparison of particle sizes and optical depths obtained at two different viewing angles (45° and 60°) for all observations in which the same cloud was seen at both angles.

uncertainty. Smaller particle sizes are generally more reliably determined than larger particle sizes; this is expected from Fig. 6, which shows that particle radii larger than $25\ \mu\text{m}$ cannot be distinguished. Emissivity errors produced by representing nonspherical crystals as equal volume-to-area-ratio spheres (discussed below) are small (Grenfell and Warren 1999; Fu et al. 1998). Optical depths are not very sensitive to errors in emissivity and t_c ; so τ_g can be reliably determined over a broad range of cloud optical thicknesses.

Figure 14 shows a comparison of particle sizes and optical depths obtained for the same clouds at two different viewing angles. As expected, the agreement is poor for particle sizes greater than $20\text{--}25\ \mu\text{m}$, whereas

smaller particle sizes determined at different viewing angles are very similar. The values can also be different if two different clouds at different heights are being viewed at the two angles.

6. Comparison with independent observations

a. Crystal sizes

Atmospheric ice crystals falling onto a gridded slide were collected at South Pole Station for 100 days from June to October of 1992 and were photographed under a microscope; an example is shown in Fig. 15. The photographs were then scanned and digitized for interactive computer analysis. Dimensions of 14 000 crystals were measured, and their surface areas and volumes were determined. For each crystal, "equivalent spheres" were determined using three different prescriptions: equal surface area, equal volume, and equal volume-to-area ratio (V/A). The third prescription is advocated by Grenfell and Warren (1999); it conserves both total area and total volume of ice in the cloud but does not conserve particle number. Other theoretical works (Foot 1988; Fu et al. 1998) favor the equal-V/A prescription. The size distribution of ice crystals in each photograph was then used to obtain three values of r_{eff} , which are compared in Fig. 16 with the particle radii obtained from spectral measurements. On average, the remotely sensed radius agrees with the equal-V/A prescription, whereas the equal-volume and equal-area radii are unrealistically large. The median r_{eff} from the photographs ($14.1\ \mu\text{m}$) is also similar to the median remotely sensed r_{eff} ($15.2\ \mu\text{m}$). This is surprising, because one would expect crystals falling out of the cloud to be larger than the average for the cloud. However, the radii from the photographs are not correlated with the remotely sensed radii. This may be due to the difference of 2–6 h between the time the crystals were collected and the time the spectral measurements were taken. The average r_{eff} is also close to what we obtain from analyzing Kikuchi and Hogan's (1979; their Fig. 7) *a*-axis and *c*-axis lengths in terms of equal-V/A spheres; $r_{\text{eff}} = 17.5\ \mu\text{m}$ for summer.

b. Cloud types

A scatter diagram of cloud optical depths and base heights is shown in Fig. 17, where the base heights were obtained from Part I. Low clouds are distributed across all optical depths, but high clouds are typically thin. Almost all the clouds with $\tau_g > 2$ had bases below 300 m.

Visual cloud observations are made every 6 h throughout the year by personnel of the South Pole Weather Office and are reported in the standard synoptic code (World Meteorological Organization 1974). The reports of cloud types can be compared with our retrieved base heights and optical thick-

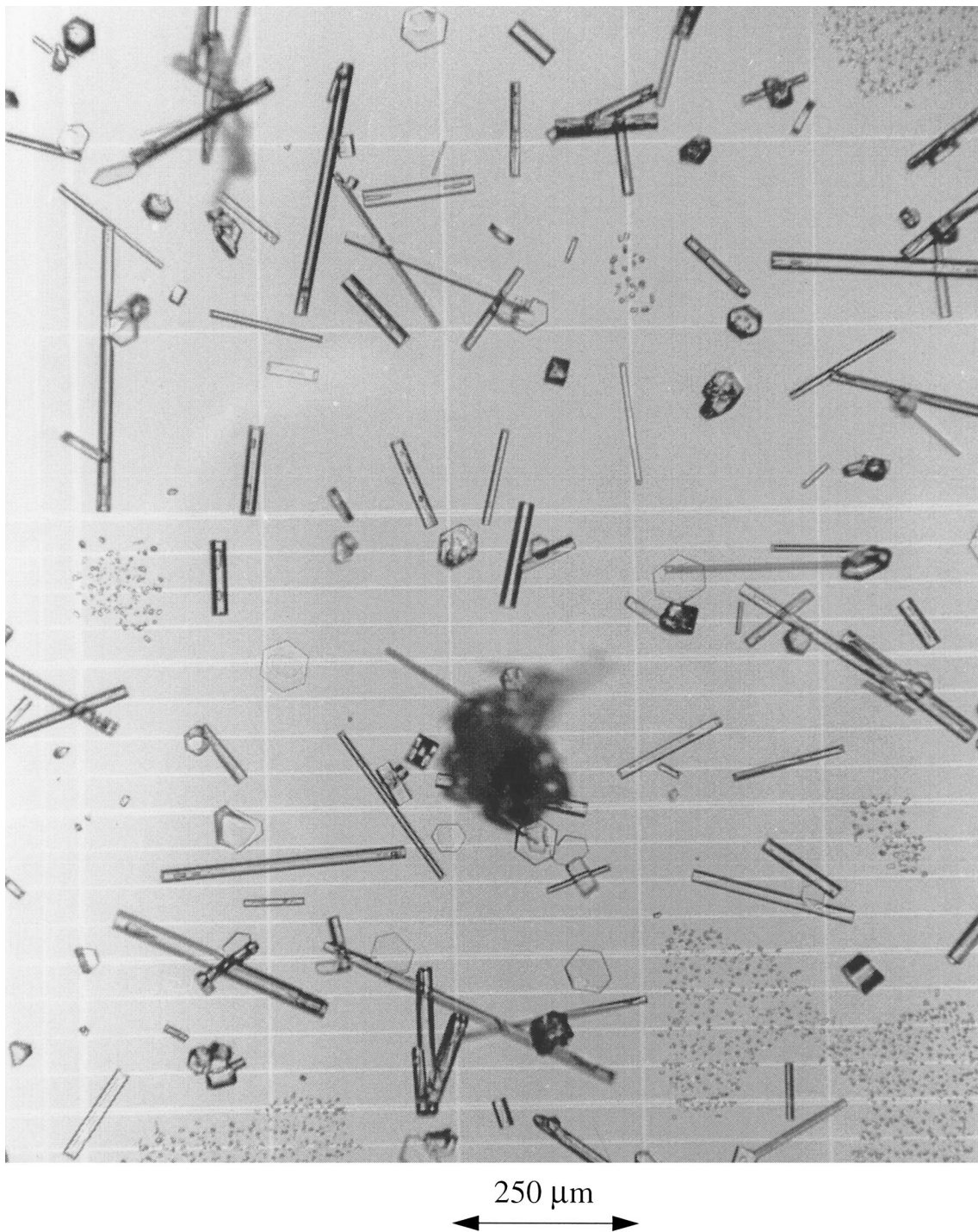


FIG. 15. Photograph of falling ice crystals at the South Pole, taken under a cloud on 5 Jul 1992. These particles were scanned and digitized, and their surface areas and volumes were computed so that they could be related to equivalent spheres of equal area ($r_A = 28 \mu\text{m}$), equal volume ($r_V = 21 \mu\text{m}$), and equal volume-to-area ratio ($r_{VA} = 16 \mu\text{m}$). All three values are larger than the particle radius obtained from the spectral measurement from that day ($11.3 \mu\text{m}$), but r_{VA} is closest.

nesses. They are in general agreement, in that the optically thicker clouds are usually reported as nimbostratus (Ns), and clouds with the highest retrieved bases are reported as cirrus (Ci) or cirrostratus (Cs).

Stratus (St) clouds tend to be reported as low, while altostratus (As) and altocumulus (Ac) are intermediate in height (other cloud types are less common). However, it is noteworthy that these cirrus clouds over the

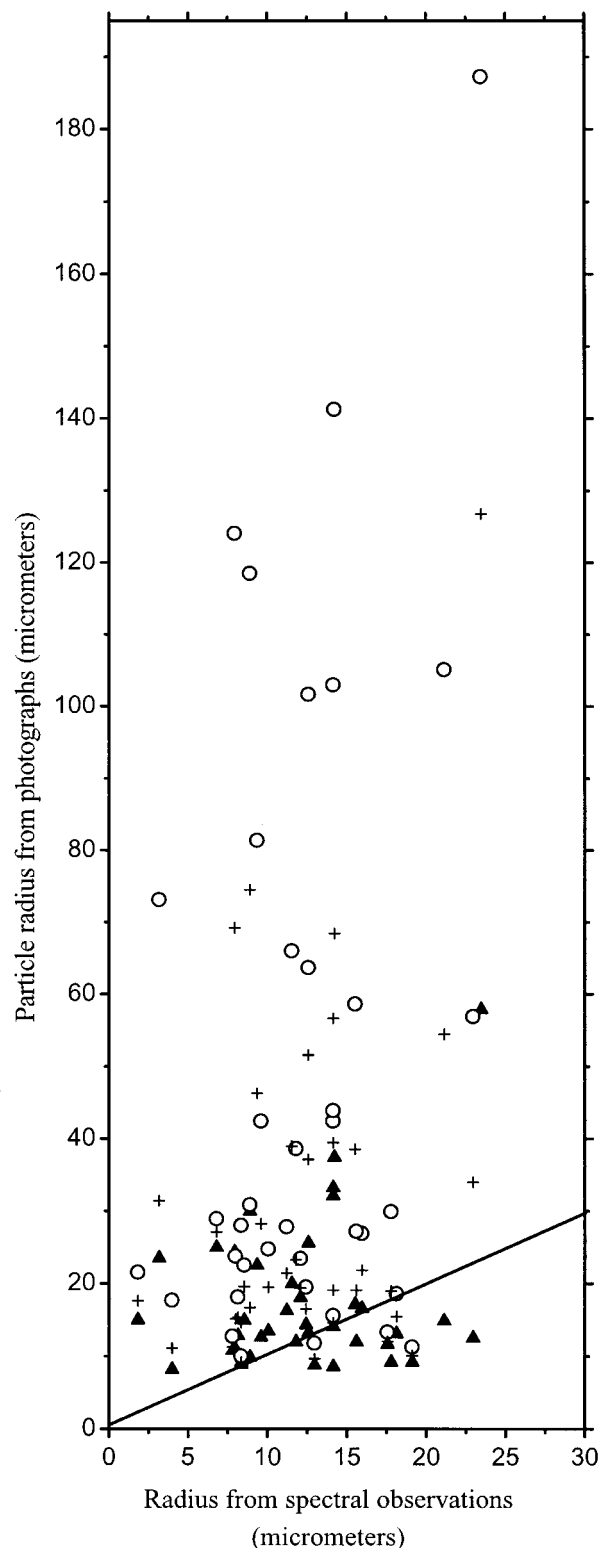


FIG. 16. Comparison of particle sizes obtained from spectral measurements with those obtained from photographs. The equivalent spherical radius for each crystal observed in the pictures was obtained in three different ways. (a) Open circles indicate the effective radii of spheres with identical surface areas to the crystals observed, (b) plus signs (+) indicate the effective radii of spheres with identical

Antarctic Plateau are much lower than cirrus elsewhere, being only 1–6 km above the surface (4–9 km above sea level). This is consistent with the low tropopause height of 8–9 km above sea level (Warren 1996; Harder et al. 2000, their Table 3).

7. Conclusions

A method has been developed for ground-based remote sensing of optical depth τ and effective ice particle radius r_{eff} for clouds over the Antarctic Plateau. To infer these two quantities the method uses three measurements: cloud emissivity at two wavelengths in the infrared atmospheric windows and cloud transmittance of emission by stratospheric ozone. The inference of τ becomes inaccurate for τ greater than 5 (Fig. 13b), so its utility is limited to thin clouds, which, however, do predominate over the Antarctic Plateau. The inference of r_{eff} becomes inaccurate for r_{eff} greater than 25 μm (Fig. 14a). We do not have independent measurements of τ that could be used to assess the accuracy of the optical depth retrieval. However, we do have direct measurements of crystal dimensions from photographs, and they are comparable to the remotely sensed effective radii if the equal-V/A prescription is used.

Cloud optical thickness over the Antarctic Plateau is considerably less than on the coast. Whereas clouds on the coast typically have τ greater than 20, nearly two-thirds of the clouds detected at the South Pole have τ less than 1. There is a seasonal cycle in optical depth on the plateau, with thick clouds being less common in winter.

Effective cloud particle radius could be estimated in 80% of the observations; in the remaining 20%, only a lower limit of 25 μm could be established. The median r_{eff} is 15.2 μm ; it is smaller in winter than in summer. This tendency is also seen in photomicrographs of falling snow crystals: the winter crystals we photographed are smaller than the summer crystals photographed by Kikuchi and Hogan (1979) and by Tape (1994).

The three tendencies we find (larger crystals in summer than in winter, larger optical depths in summer than in winter, and larger optical depths at the coast than in the interior) conform to expectation, because the atmosphere contains more water vapor at the coast than in the interior and more water vapor in summer than in winter.

Note added in proof: Direct sampling of cloud particles from a tethered balloon at South Pole Station in a recent field experiment (summer 2000/01) has shown several examples of clouds consisting mostly or entirely of supercooled liquid water droplets at temperatures

←

volumes, and (c) solid triangles indicate the effective radii of spheres with identical surface-to-volume ratios. The solid straight line shows a slope of 1.

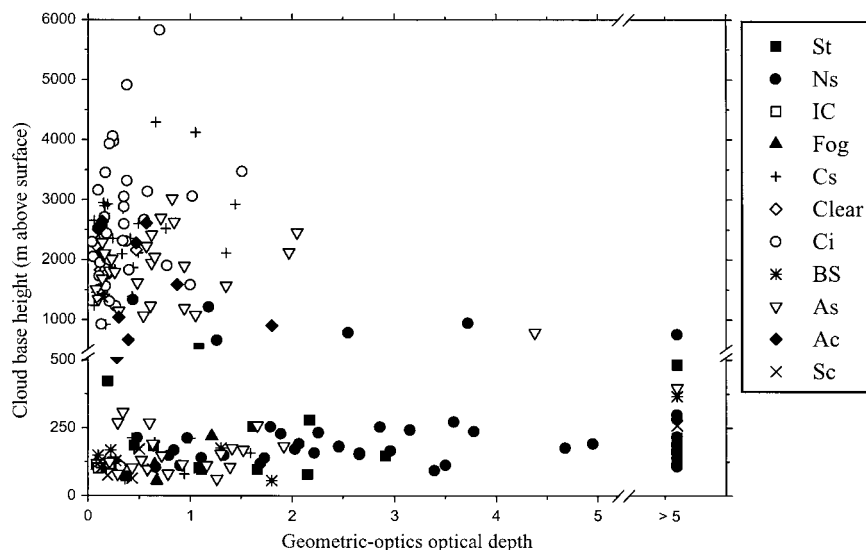


FIG. 17. Cloud-base heights and optical depths at the South Pole from 1992 (clouds below 500 m are plotted on an expanded vertical scale). High clouds are typically thinner than low clouds, and low clouds have a larger range of optical depths. All the thick clouds are based within 1 km of the surface. The symbols indicate the cloud types reported by the South Pole Weather Office observers (see text). In addition, a few cloudy spectra were also measured under other conditions, namely fog, blowing snow (BS), and falling ice crystals (IC), as well as one observation taken under reportedly clear skies.

−25° to −35°C. Such water clouds are likely to have occurred in 1992 as well during the summer season (December–January). Our inference of τ_g and r_{eff} in summer may be sensitive to the assumption of ice phase; this question will be examined in future work.

Acknowledgments. Elizabeth Tuttle analyzed the photographs of falling ice crystals taken at the South Pole in 1992. NOAA/CMDL provided ozonesonde data, and the South Pole Weather Office provided radiosonde data and synoptic cloud reports. We thank Steven Neshyba and Qiang Fu for helpful discussions and Tom Grenfell and Norman McCormick for commenting on an earlier draft of this manuscript. This research was supported by NSF Grants OPP-94-21096 and OPP-97-26676.

REFERENCES

- Clough, S. A., M. J. Iacono, and J. L. Moncet, 1992: Line-by-line calculations of atmospheric fluxes and cooling rates: Application to water vapor. *J. Geophys. Res.*, **97**, 15 761–15 785.
- Collard, A. D., S. A. Ackerman, W. L. Smith, X. Ma, H. E. Revercomb, R. O. Knuteson, and S.-C. Lee, 1995: Cirrus cloud properties derived from high spectral resolution infrared spectrometry during FIRE II. Part III: Ground-based HIS results. *J. Atmos. Sci.*, **52**, 4264–4275.
- DeSlover, D. H., W. L. Smith, P. K. Piironen, and E. W. Eloranta, 1999: A methodology for measuring cirrus cloud visible-to-infrared optical depth ratios. *J. Atmos. Oceanic Technol.*, **16**, 251–262.
- Dozier, J., and S. G. Warren, 1982: Effect of viewing angle on the infrared brightness temperature of snow. *Water Resour. Res.*, **18**, 1424–1434.
- Foot, J. S., 1988: Some observations of the optical properties of clouds, II, cirrus. *Quart. J. Roy. Meteor. Soc.*, **114**, 145–164.
- Fu, Q., P. Yang, and W. B. Sun, 1998: An accurate parameterization of the infrared radiative properties of cirrus clouds for climate models. *J. Climate*, **11**, 2223–2237.
- Grenfell, T. C., 1998: Evolution of electromagnetic signatures of sea ice from initial formation to establishment of thick first-year ice. *IEEE Trans. Geosci. Remote Sens.*, **36**, 1642–1654.
- , and S. G. Warren, 1999: Representation of a nonspherical ice particle by a collection of independent spheres for scattering and absorption of radiation. *J. Geophys. Res.*, **104**, 31 697–31 709.
- Grund, C. J., S. A. Ackerman, E. W. Eloranta, R. O. Knuteson, H. E. Revercomb, W. L. Smith, and D. P. Wylie, 1990: Cirrus cloud characteristics derived from volume imaging lidar, high spectral resolution lidar, HIS radiometer, and satellite. Preprints, *Seventh Conf. on Atmospheric Radiation*, San Francisco, CA, Amer. Meteor. Soc., 357–362.
- Hansen, J. E., and L. D. Travis, 1974: Light scattering in planetary atmospheres. *Space Sci. Rev.*, **16**, 527–610.
- Harder, S., S. G. Warren, and R. J. Charlson, 2000: Sulfate in air and snow at the South Pole: Implications for transport and deposition at sites with low snow accumulation. *J. Geophys. Res.*, **105**, 22 825–22 832.
- Houghton, J. T., 1991: *The Physics of Atmospheres*. Cambridge University Press, 271 pp.
- Kikuchi, K., and A. W. Hogan, 1979: Properties of diamond dust type ice crystals observed in summer season at Amundsen–Scott South Pole Station, Antarctica. *J. Meteor. Soc. Japan*, **57**, 180–190.
- Lacis, A. A., J. E. Hansen, and M. Sato, 1992: Climate forcing by stratospheric aerosols. *Geophys. Res. Lett.*, **19**, 1607–1612.
- Lubin, D., 1994: Infrared properties of the maritime Antarctic atmosphere. *J. Climate*, **7**, 121–140.
- , and D. A. Harper, 1996: Cloud radiative properties over the South Pole from AVHRR infrared data. *J. Climate*, **9**, 3405–3418.
- , B. Chen, D. H. Bromwich, R. C. J. Somerville, W. Lee, and K. M. Hines, 1998: The impact of Antarctic cloud radiative properties on a GCM climate simulation. *J. Climate*, **11**, 447–462.
- Mahesh, A., V. P. Walden, and S. G. Warren, 2001: Ground-based

- infrared remote sensing of cloud properties over the Antarctic Plateau. Part I: Cloud base heights. *J. Appl. Meteor.*, **40**, 1265–1278.
- Morley, B. H., E. E. Uthe, and W. Viezee, 1989: Airborne lidar observations of clouds in the Antarctic troposphere. *Geophys. Res. Lett.*, **16**, 491–494.
- Ricchiazzi, P., C. Gautier, and D. Lubin, 1995: Cloud scattering optical depth and local surface albedo in the Antarctic: Simultaneous retrieval using ground-based radiometry. *J. Geophys. Res.*, **100**, 21 091–21 104.
- Simmonds, I., 1990: Improvements in general circulation model performance in simulating Antarctic climate. *Antarc. Sci.*, **2**, 287–300.
- Smith, W. L., X. L. Ma, S. A. Ackerman, H. E. Revercomb, and R. O. Knuteson, 1993: Remote sensing cloud properties from high spectral resolution infrared observations. *J. Atmos. Sci.*, **50**, 1708–1720.
- Stamnes, K., S.-C. Tsay, W. Wiscombe, and K. Jayaweera, 1988: A numerically stable algorithm for discrete-ordinate-method radiative transfer in multiple scattering and emitting layered media. *Appl. Opt.*, **27**, 2502–2509.
- Stone, R. S., 1993: Properties of austral winter clouds derived from radiometric profiles at the South Pole. *J. Geophys. Res.*, **98**, 12 961–12 971.
- Tape, W., 1994: *Atmospheric Halos*. Amer. Geophys. Union, 143 pp.
- Walden, V. P., 1995: The downward longwave radiation spectrum over the Antarctic Plateau. Ph.D. thesis, Geophysics Program, University of Washington, 267 pp.
- , S. G. Warren, and F. J. Murcray, 1998: Measurements of the downward longwave radiation spectrum over the Antarctic Plateau and comparisons with a line-by-line radiative transfer model for clear skies. *J. Geophys. Res.*, **103**, 3825–3846.
- Warren, S. G., 1984: Optical constants of ice from the ultraviolet to the microwave. *Appl. Opt.*, **23**, 1206–1225.
- , 1996: Antarctica. *Encyclopedia of Climate and Weather*, S. H. Schneider, Ed., Oxford University Press, 32–39.
- Wiscombe, W. J., 1979: Mie scattering calculations: Advances in technique and fast, vector-speed computer codes. NCAR Tech. Note TN-140+STR, 91 pp. [NTIS PB 301388.]
- , 1980: Improved Mie scattering algorithms. *Appl. Opt.*, **19**, 1505–1509.
- World Meteorological Organization, 1974: *Manual on Codes*. Vol. 1, WMO Publ. 306, 348 pp.